An Improved Model-Free Predictive Current Control for SPMSM Drives Based on Adaptive Extended State Observer With Robust Sliding Mode Speed Controller

Changliang Dang, Manfeng Dou, *Member, IEEE*, Shuhao Yan, Mengxi Dang,
Dongdong Zhao, *Member, IEEE*, and Zhiguang Hua, *Member, IEEE*

***Abstract*—Conventional ultralocal model-based model-free predictive current control using an extended state observer (ESO) based on an ultralocal model significantly promotes the robustness against motor parameter mismatch. However, a large bandwidth of ESO leads to an enhanced disturbance rejection capability, but the noise suppression performance will deteriorate. To address this issue, an adaptive extended state observer (AESO) with an adaptive bandwidth tuning scheme based on the estimated error was proposed, in which the observer bandwidth is automatically adjusted to reduce the estimation errors of system states and total uncertainty against the measurement noise. Accordingly, the different requirements of observer bandwidth under various operating conditions can be satisfied, and the performance of disturbance rejection and noise suppression is balanced. Moreover, the stability of the proposed AESO is proved based on the Lyapunov method. Furthermore, to improve the dynamic performance and robustness of the speed loop, a robust sliding mode speed controller based on a novel reaching law and a sliding mode observer is proposed to replace the conventional proportional-integral. The comparative experiments on a 1.9 kW surface-mounted permanent magnet synchronous motor are conducted to validate the superiority of the proposed control methods compared with traditional methods.**

***Index Terms*—Adaptive extended state observer (AESO), model-free predictive current control (MFPCC), robustness, sliding mode control, ultralocal model.**

I. INTRODUCTION

A. Motivation

RECENTLY, due to their advantages, such as high power density, simple structure, excellent control performance, and good reliability, surface-mounted permanent magnet synchronous motors (SPMSMs) have been widely used in many industrial applications, such as robot drives, electrification transportation, and electric vehicles [1], [2]. High-performance speed and current control are essential for the optimal operation of SPMSMs. They influence steady-state and transient performance and even system stability. Accordingly, it is crucial to simultaneously improve the performance of both the internal current and external speed loop for SPMSM drives.

B. Literature Review

With the rapid development of control theory, in addition to linear control represented by PI, active disturbance rejection control (ADRC) [3], sliding mode control (SMC) [4], predictive control (PC) [5], [6], [7], have become research hotspots. In particular, the PC has attracted extensive attention owing to its intuitive structure and exceptional dynamic performance. The control accuracy of the PC depends on the precise model of the controlled object. However, the performance will degrade due to parameter variation and external disturbance [8].

To fundamentally solve this problem, model-free predictive current control (MFPCC) receives widespread attention and is still developing. Compared to the traditional methods, MFPCC provides remarkable response performance and enhanced robustness against disturbances. In [9], a model-free control method that only used the system input and output information was proposed. In [10], an enhanced extended state observer (ESO) was developed to identify the inductance of SPMSM and achieve model-free control. However, the high bandwidth of ESO amplifies noise, while low bandwidth results in poor convergence. Hence, the adaptive extended state observer (AESO) is an attractive choice for simultaneously coordinating antidisturbance performance and noise suppression.

In [11], a scalable-bandwidth extended state observer (SESO) was proposed to evaluate the time-varying total disturbance in a wastewater treatment process (WWTP), which lacks parameter tuning guidance and experimental validation. Rsetam et al. [12] proposed an adaptive ADRC with a continuous sliding mode component for electric heating furnace (EHF) systems. Due to the bandwidth functions adaptively adjusting the ESO and

Received 23 January 2025; revised 24 March 2025; accepted 19 April 2025. Date of publication 5 May 2025; date of current version 30 June 2025. This work was supported in part by the National Natural Science Foundation of China under Grant 52307251 and Grant 52277226, and in part by Shaanxi Postdoctoral Science Foundation under Grant 2024BSHSDZZ226. Recommended for publication by Associate Editor B. Singh. *(Corresponding author: Zhiguang Hua.)*

The authors are with the School of Automation, Northwestern Polytechnical University (NWPU), Xi'an 710072, China (e-mail: dcl312@mail.nwpu.edu.cn; doumf@nwpu.edu.cn; zgysh2020@mail.nwpu.edu.cn; dangmx@mail.nwpu.edu.cn; zhaodong@nwpu.edu.cn; zhiguang.hua@nwpu.edu.cn).

Color versions of one or more figures in this article are available at https://doi.org/10.1109/TPEL.2025.3564997.

Digital Object Identifier 10.1109/TPEL.2025.3564997

controller gains within the ADRC technique, the noise amplification caused by high gain can be solved. A finite-time adaptive extended state observer was proposed in [13], which adopted the system error to adjust the observer bandwidth gain. However, the adaptive bandwidth of ESO only switched between the two alternative values, so the adaptive range was limited. In [14], an adaptive ADRC scheme was proposed for precise angular steering position tracking of the uncertain and nonlinear SBW system. The observer gains could be dynamically adjusted based on the estimation error to achieve a good estimation performance. In [15], two ESOs with an adaptive bandwidth were designed to estimate the extended electromagnetic force (EEMF) over a wide speed range. In [16], an ultralocal model based on the rotating coordinate system was developed by utilizing an AESO to enhance the accuracy of MFPCC. However, little work has been done on the stability analysis of the AESO. In [17], an adaptive law was designed to switch between the classical extended state observer and reduced-order generalized proportional integral observer under different working conditions. However, the control performance relies on the switching algorithm, and the computational burden cannot be ignored. In [18], an adaptive integral extended state observer (AIESO) was proposed to balance the disturbance rejection and noise suppression of the traditional ESO. However, although there was a detailed analysis process for the stability of AESO, the control system will be influenced by the perturbation of PMSM parameters, especially the inductance. Additionally, the traditional linear controller was selected as the speed controller, and the dynamic response and robustness can be further promoted. In [19], an adaptive gain ESO was proposed to reduce the torque ripple and improve current distortion. However, the steady-state performance and dynamic response were not considered. In [20], an adaptive switching fourth-order LESO was proposed to achieve high estimation accuracy for disturbance and strong immunity to measurement noise. However, the increase in observer order demands higher storage capacity and arithmetic ability from the digital processor. Although the performance of ESO has been improved after continuous research, more effective strategies still need to be developed in terms of robustness, dynamic response, and steady-state performance.

As for the speed controller, in the existing literature on MFPCC, such as [9] and [10], both adopt traditional linear PI as the speed controllers. However, the existing nonnegligible disturbances in the speed regulation system of PMSM, such as parameter perturbations, system uncertainties, and external disturbances, will deteriorate the speed contrl performance.

So far, various nonlinear methods have recently been developed to replace the PI for SPMSM drives. In [21], a model predictive direct speed control (MPDSC) strategy was proposed to promote the dynamic performance of SPMSM. However, the cost function of MPDSC is too complex, and the computation burden problem cannot be ignored. In [22], an adaptive speed control method was proposed, but the robustness was affected. In [23], an ADRC controller using a phase-locking loop observer (PLLO) for speed control was proposed, but the PLLO was more susceptible to system noises. In addition to the above methods, the sliding-mode control (SMC) has been successfully applied due to the advantages of good dynamic response and strong robustness [24]. However, the inherent drawback of SMC is the chattering phenomenon, which leads to discontinuous action in the control signal. In [25], an extreme learning machine (ELM)-based super-twisting integral terminal sliding mode control (STITSMC) was proposed to improve the speed control performance and suppress the chattering. Moreover, the reaching law strategy is an attractive solution to alleviate the chattering due to its direct impact on the reaching process [26]. In [27], a new reaching law combined with the hyperbolic tangent function was designed to weaken the chattering. In [4], a hybrid reaching law-based sliding mode speed controller was proposed, incorporating an exponential plus proportional term to suppress chattering. In [28], a terminal sliding mode reaching law (TRL) was proposed to obtain finite convergence and reduce the chattering. In [29], an enhanced exponential reaching law (EERL) was proposed to improve the performance of the exponential reaching law (ERL).

C. Contribution

This article proposes an AESO-MFPCC and a robust sliding mode speed controller (RSMSC) to improve the performance of the conventional ESO-MFPCC. The main contributions are listed as follows.

1) An AESO is proposed to balance the antidisturbance capability and noise suppression. The ESO-MFPCC in [9] requires bandwidth adjustment, which is time consuming and laborious. In contrast, the proposed AESO-MFPCC only needs to set the upper and lower bandwidth limits, satisfying the demand under different working conditions.
2) Compared with DPCC, the current tracking error is eliminated due to the compensation of AESO. Compared with [7], precise motor parameters are not required, significantly enhancing robustness to parameter perturbation.
3) By combining a novel reaching law (NRL) and a sliding mode observer (SMO), the RSMSC is proposed to improve speed control performance. Moreover, the execution time of the digital controller is less than half of the sampling period, making it suitable for practical applications.

D. Article Organization

The rest of this article is organized as follows. Section II demonstrates the problem and introduces the mathematical model. The proposed AESO-MFPCC is presented in Section III. The proposed RSMSC is introduced in Section IV. The comparison of experiment results is provided in Section V. Finally, Section VI concludes this article.

II. PROBLEM DESCRIPTION

A. Mathematical Model of SPMSM

Assuming that the stator windings of the SPMSM are three-phase symmetrical in space and the magnetic circuit is not saturated, and neglecting the iron losses, hysteresis loss, and magnet eddy current loss, the mathematical model of SPMSM in dq-axis coordinate can be given as

$$\begin{cases} \frac{di_d}{dt} = \frac{u_d}{L_s} - \frac{R_s}{L_s} i_d + \omega_e i_q \\ \frac{di_q}{dt} = \frac{u_q}{L_s} - \omega_e i_d - \frac{R_s i_q}{L_s} - \frac{\psi_f}{L_s} \omega_e \end{cases} \tag{1}$$

where u_d and u_q are the dq-axis voltages; R_s and L_s are the stator resistance and inductance; ψ_f is the flux linkage, with ω_e the electrical angular velocity.

The motion equation of SPMSM can be given as

$$J\dot{\omega}_m = T_e - B\omega_m - T_L \tag{2}$$

where ω_m is the mechanical velocity, satisfying $\omega_e = n_p \omega_m$, with n_p the number of pole pairs; T_e is the electromagnetic torque; T_L, B, and J are the external load torque, the viscous friction coefficient, and the moment of inertia, respectively.

B. Conventional ESO-Based MFPCC

The ESO-MFPCC control scheme based on the ultralocal model was proposed in [9]. Due to the uncertainty estimated and compensated by ESO, the model-free control can be achieved. The ultralocal model of SPMSM is given as

$$\begin{cases} \frac{di_d}{dt} = \alpha_s u_d + F_d \\ \frac{di_q}{dt} = \alpha_s u_q + F_q \end{cases} \tag{3}$$

where α_s denotes the gain of control input obtained through experience; F_d and F_q represent the unknown disturbance on the dq-axis, which must be updated online and needs to be estimated by observers, containing the known structure, unknowns, and some system disturbances.

Suppose the unknown disturbance is bounded, and take the d-axis as an example, define $x_{1d} = i_d$, $x_{2d} = F_d$, then the d-axis part of (3) can be rewritten as

$$\begin{cases} \dot{x}_{1d} = \alpha_s u_d + x_2 \\ \dot{x}_{2d} = \hbar \end{cases} \tag{4}$$

where $\hbar$ denotes the derivative of F_d with respect to time.

Then the linear fixed-gain ESO can be designed as

$$\begin{cases} \dot{z}_{1d} = \alpha_s u_d + z_{2d} - \beta_1 (z_{1d} - x_{1d}) \\ \dot{z}_{2d} = -\beta_2 (z_{1d} - x_{1d}) \end{cases} \tag{5}$$

where z_{1d} and z_{2d} are the estimated values of x_{1d} and x_{2d}; β_1 and β_2 represent the observer gains, which should be reasonably designed to ensure the stability of linear ESO.

By subtracting (5) from (4), the dynamic error equation of ESO can be expressed as

$$\begin{cases} \dot{e}_{1d} = -\beta_1 e_{1d} + e_{2d} \\ \dot{e}_{2d} = -\beta_2 e_{1d} + \hbar \end{cases} \tag{6}$$

where $e_{1d} = x_{1d} - z_{1d}$ and $e_{2d} = x_{2d} - z_{2d}$.

Rewrite (6) into the state space equation as follows:

$$\dot{\boldsymbol{e}}_d = \boldsymbol{A}_d \boldsymbol{e}_d + \boldsymbol{B}_d \hbar \tag{7}$$

where $\boldsymbol{e}_d = [e_{1d} \quad e_{2d}]^T$, $\boldsymbol{A}_d = \begin{pmatrix} -\beta_1 & 1 \\ -\beta_2 & 0 \end{pmatrix}$, $\boldsymbol{B}_d = [0 \quad 1]^T$.

Thus, the characteristic polynomial of the error dynamic equation shown in (7) can be expressed as

$$P(s) = s^2 + \beta_1 s + \beta_2. \tag{8}$$

To ensure the stability of ESO, all eigenvalues of the eigenequation for (8) should have negative real parts. When the eigenvalues are satisfied $\lambda_1 = \lambda_2 = -\omega_0$, and $\omega_0 > 0$, (8) can be rewritten as

$$P(s) = (s + \omega_0)^2 = s^2 + 2\omega_0 s + \omega_0^2. \tag{9}$$

By comparing (8) and (9), $\beta_1 = 2\omega_0$ and $\beta_2 = \omega_0^2$ can be obtained. The above analysis shows that the estimated values z_{1d} and z_{2d} can be obtained when the observer gains β_1 and β_2, which can be selected appropriately. Meanwhile, neither the ultralocal model nor the linear fixed-gain ESO includes any electrical parameters of SPMSM. The MFPCC method, based on traditional linear fixed-gain ESO, eliminates the influence of model parameter perturbations. However, the control performance of MFPCC will be directly affected by the ESO observation performance.

By applying the Laplace transform, (5) can be expressed as

$$\begin{cases} s z_{1d} = \alpha_s u_d + z_{2d} - \beta_1 (z_{1d} - x_{1d}) \\ s z_{2d} = -\beta_2 (z_{1d} - x_{1d}). \end{cases} \tag{10}$$

Rearrange (10), one can get

$$\begin{cases} z_{1d} = \frac{\alpha_s s}{s^2 + \beta_1 s + \beta_2} u_d + \frac{\beta_2 + \beta_1 s}{s^2 + \beta_1 s + \beta_2} x_{1d} \\ z_{2d} = \frac{-\alpha_s \beta_2}{s^2 + \beta_1 s + \beta_2} u_d + \frac{\beta_2 s}{s^2 + \beta_1 s + \beta_2} x_{1d}. \end{cases} \tag{11}$$

To more accurately analyze the control performance of traditional linear fixed-gain ESO, the following four scenarios are taken into account.

1) Consider the perturbation effect on the estimate z_{1d}. The transfer function between the input disturbance u_d and the estimated value z_{1d} can be obtained as follows:

$$\frac{z_{1d}(s)}{u_d(s)} = \frac{\alpha_s s}{s^2 + \beta_1 s + \beta_2}. \tag{12}$$

2) Consider the noise effect on the estimate z_{1d}. The transfer function between the noise introduced by the observed quantity i_d and the estimated value z_{1d} can be obtained as follows:

$$\frac{z_{1d}(s)}{x_{1d}(s)} = \frac{\beta_2 + \beta_1 s}{s^2 + \beta_1 s + \beta_2}. \tag{13}$$

3) Consider the perturbation effect on the estimate z_{2d}. The transfer function between the input disturbance u_d and the estimated value z_{2d} can be obtained as follows:

$$\frac{z_{2d}(s)}{u_d(s)} = \frac{-\alpha_s \beta_2}{s^2 + \beta_1 s + \beta_2}. \tag{14}$$

4) Consider the noise effect on the estimate z_{2d}. The transfer function between the noise introduced by the observation i_d and the estimated value z_{2d} can be obtained as follows:

$$\frac{z_{2d}(s)}{x_{1d}(s)} = \frac{\beta_2 s}{s^2 + \beta_1 s + \beta_2}. \tag{15}$$

Moreover, the Bode diagram corresponding to (12), (13), (14), and (15) is shown in Fig. 1. It is evident from Fig. 1(a) that when a higher observer gain is selected, there is a strong immunity to low-frequency perturbations. However, the effect of high gain on noise suppression is poor, as shown in Fig. 1(b).

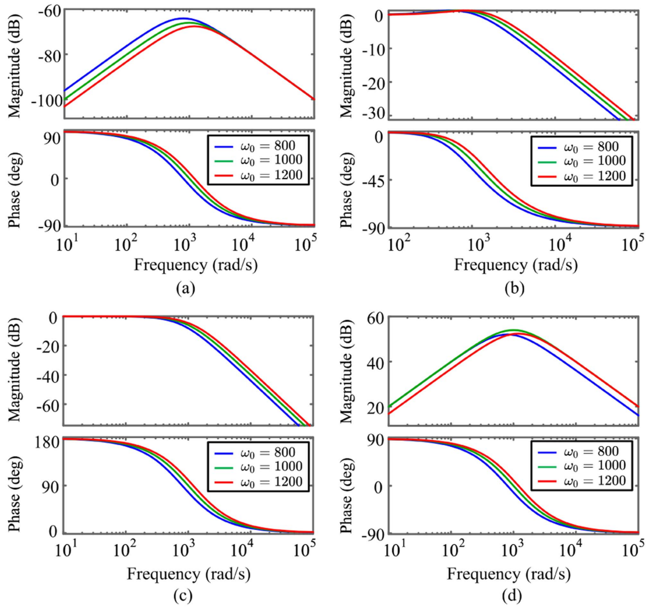

Fig. 1. Bode diagram of ESO. (a) z_{1d}/u_d. (b) z_{1d}/x_{1d}. (c) z_{2d}/u_d. (d) z_{2d}/x_{1d}.

Furthermore, it can be seen in Fig. 1(c) that the low-frequency antidisturbance performance is the same when different gains are selected. Similar to the conclusion in Fig. 1(b), the noise suppression performance gradually decreases with the increase of observer gain, as shown in Fig. 1(d). Thus, it can be concluded that high gain can enhance the antidisturbance capability but inevitably magnify the measurement noise. Meanwhile, relatively high observer gains are often adopted due to the strong immunity. However, the estimation efficiency is affected by the measurement noise in practical applications, which is amplified by the high gain.

Therefore, based on the above analysis, a novel AESO is proposed to achieve a dynamic balance between disturbance rejection performance and noise suppression. Furthermore, ESO-MFPCC usually adopts the PI control scheme as the speed controller; the limitations of the PI control method were comprehensively analyzed in [30], and it can be concluded that it is difficult to achieve a remarkable dynamic responsiveness and antidisturbance performance simultaneously.

III. DESIGN OF SPEED CONTROLLER

This section develops the proposed RSMSC, which combines an integral terminal sliding mode surface, the proposed NRL, and an SMO.

A. Model Description of Speed Loop

Considering the parameters variation and unknown disturbance, (2) can be rewritten as

$$\dot{\omega}_m = \frac{3n_p\psi_{f0}}{2J_0} i_q - \frac{B\omega_m}{J_0} - \frac{T_L}{J_0} + f_\omega$$

$$- \frac{1}{J_0}(\Delta J\dot{\omega}_m - 3n_p\Delta\psi_f/2 + \Delta B\omega_m) \tag{16}$$

where the parameters with "Δ" denote the variation values between the nominal and actual values; f_ω is the unknown interference.

Then the motion equation of SPMSM can be rewritten as

$$\dot{\omega}_m = bi_q + F_\omega \tag{17}$$

where $b = \frac{3n_p\psi_{f0}}{2J_0}$ is the control gain and $F_\omega = -\frac{B\omega_m}{J_0} - \frac{T_L}{J_0} - \frac{1}{J_0}(\Delta J\dot{\omega}_m - 3n_p\Delta\psi_f/2 + \Delta B\omega_m) + f_\omega$ is considered as the lumped disturbance, including parameters perturbation and unknown interference.

B. SMO Design

According to (17), an SMO can be established as

$$\begin{cases} \dot{\hat{\omega}}_m = bi_q + \hat{F}_\omega + u_{smo} \\ \dot{\hat{F}}_\omega = lu_{smo} \end{cases} \tag{18}$$

where l denotes the feedback gain of SMO and u_{smo} is the SMC function. $\hat{\omega}_m$ and $\hat{F}_\omega$ are the estimated values of ω_m and F_ω, respectively. The error dynamics can be derived by subtracting (17) from (18) as

$$\begin{cases} \dot{\tilde{\omega}}_m = \tilde{F}_\omega + u_{smo} \\ \dot{\tilde{F}}_\omega = lu_{smo} \end{cases} \tag{19}$$

where $\tilde{\omega}_m = \hat{\omega}_m - \omega_m$ and $\tilde{F}_\omega = \hat{F}_\omega - F_\omega$ represent the estimated errors. By selecting the sliding mode surface as $\sigma = \tilde{\omega}$, the switching signal u_{smo} can be designed as

$$u_{smo} = -\nu \mathrm{sgn}(\sigma) \tag{20}$$

where ν is the designed positive gain, with sgn(*) the symbolic function. The stability analysis is similar to the sliding mode load torque observer in [31], which is omitted here.

C. RSMSC

The TRL was proposed in [28], which can be expressed as

$$\dot{s} = -\eta_1 s - \eta_2 |s|^\lambda \mathrm{sgn}(s) \tag{21}$$

where $\eta_1 > 0$, $\eta_2 > 0$, $0 < \lambda < 1$.

Moreover, the EERL was proposed in [29], which can be expressed as

$$\begin{cases} \dot{s} = -\eta_3 s - \frac{\eta_4}{D(s)}|s|^\gamma \mathrm{sgn}(s) \\ D(s) = \alpha + (1-\alpha)e^{-\beta|s|} \end{cases} \tag{22}$$

where $\eta_3 > 0$, $\eta_4 > 0$, $\beta > 0$, $0 < \alpha < 1$, and $0 < \gamma < 1$.

In this section, to further improve the speed control performance of SPMSM drives, the NRL is given as

$$\begin{cases} \dot{s} = -k_1 s|s|^\delta - k_2 r(s)\frac{1}{\theta + \rho e^{-\mu|s|}} \\ r(s) = \begin{cases} \mathrm{sgn}(s) & |s| \geq \Delta \\ \tanh(\varsigma s) & |s| < \Delta \end{cases} \end{cases} \tag{23}$$

where k_1, k_2, θ, ρ, and μ are positive control gains. $0 < \delta < 1$, $\varsigma = 2\pi/\Delta$, $r(s)$ represents the enhanced switching function, and Δ denotes the thickness of the boundary layer.

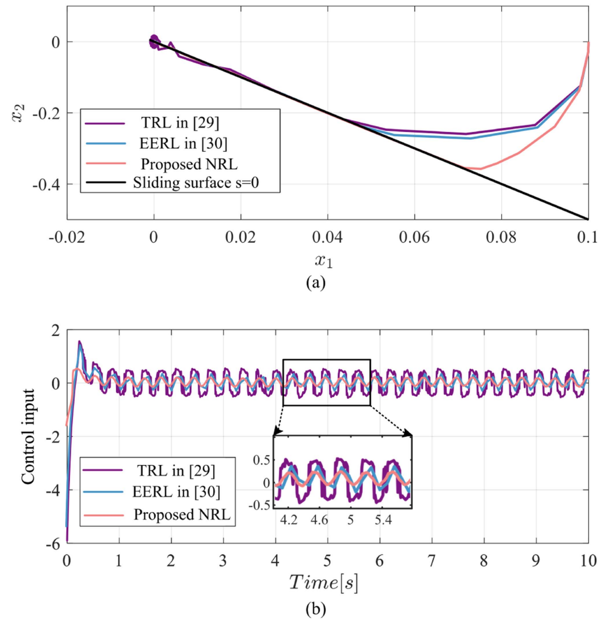

(a)

(b)

Fig. 2. Performance comparison. (a) Phase plane trajectory response performance. (b) Control input.

The symbolic function is usually adopted as the switching function in the conventional SMC, leading to the chattering phenomenon. To solve the issue, a hyperbolic tangent function with a variable boundary layer replaces the symbolic function, which successfully alleviates the discontinuity problem, especially when the system state approaches the sliding manifold. The analysis of the proposed NRL is shown as follows:

Assuming the initial state $s_0 < 1$, the analysis can be divided into three stages as follows.

Stage 1: During the process $s_0 \to s = 1$, the values of the two terms are close, so the system state can quickly approach the sliding manifold. Meanwhile, with the sliding surface decreasing, the first and second terms also decrease so that the chattering can be suppressed effectively.

Stage 2: When the state reaches the boundary layer, i.e., $\Delta \leq |s| < 1$, with the first term decreasing quickly, the second term plays a dominant role so that a certain approaching velocity is guaranteed.

Stage 3: When the state enters the boundary layer, due to the hyperbolic tangent function being utilized, the sliding mode trajectory is continuous, greatly alleviating the chattering.

Numerical simulations are carried out in MATLAB, and the reaching laws in [28] and [29] are selected as the comparative methods. The system is designed as $\dot{x}_1 = x_2$, $\dot{x}_2 = 0.1\sin(20t) + u$. The sliding surface is $s = 5x_1 + x_2$. The control input can be derived based on the sliding surface and reaching law. Fig. 2 shows the phase plane trajectory and control input. Note that the proposed NRL exhibits the fastest convergence speed and the best chattering suppression.

Then, the state variable for the speed controller is defined as $x = \omega_m^* - \omega_m$, and the sliding mode surface is selected as

$$s = x + c\int_0^t |x|^{\phi}\mathrm{sgn}(x)d\tau \tag{24}$$

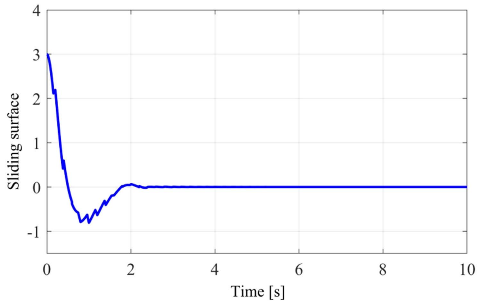

Fig. 3. Performance of the sliding surface (24).

where $c > 0$ and $0 < \phi < 1$.

By combining (17), (23), and (24), the control input can be obtained as

$$i_q = \frac{1}{b} \times \left(\dot{\omega}_m^* + c|x|^{\phi}\mathrm{sgn}(x) + k_1 s|s|^{\delta} + k_2 r(s)\frac{1}{\theta + \rho e^{-\mu|s|}} - \hat{F}_{\omega}\right) \tag{25}$$

where $r(s) = \begin{cases} \mathrm{sgn}(s) & |s| \geq \Delta \\ \tanh(\varsigma s) & |s| < \Delta \end{cases}$.

In addition, to analyze the stability, by combining (17) and (25), one can get

$$\dot{s} = -k_1 s|s|^{\delta} - k_2 r(s)\frac{1}{\theta + \rho e^{-\mu|s|}} + \hat{F}_{\omega} - F_{\omega} \tag{26}$$

where $r(s) = \begin{cases} \mathrm{sgn}(s) & |s| \geq \Delta \\ \tanh(\varsigma s) & |s| < \Delta. \end{cases}$

Thus, when the estimated error of SMO is bounded, and according to [32], the sliding manifold s will converge to 0 in a finite time. Once x reaches the sliding manifold, we have

$$x = -c\int_0^t |x|^{\phi}\mathrm{sgn}(x)d\tau. \tag{27}$$

This article combines the integral sliding mode algorithm with the terminal sliding mode algorithm to avoid the requirement for speed derivative information. In addition, the nonlinear terms are introduced to improve the convergence process. According to the finite-time stability theory, the system state can reach the designed integral sliding mode surface under any initial conditions, and the actual speed will converge to the reference speed in a finite time.

Furthermore, it can be seen from (24) that the sliding mode surface consists of tracking error and integral terms. When $s = 0$ and the system state does not reach the equilibrium point, the tracking error converges faster under the combined action of the two terms; When the system state approaches the equilibrium point, the steady-state error can be eliminated by the integral term. The reaching time can be obtained by solving (27) as $t = |x(t_0)|^{1-\phi}/(c(1-\phi))$. The numerical simulation results of the convergence of the sliding mode surface (24) are shown in Fig. 3.

IV. DESIGN OF CURRENT CONTROLLER

A. MFPCC Based on Ultralocal Model

By defining f_d and f_q the system disturbances on dq-axis, and considering the disturbance caused by SPMSM parameter mismatch and unmodeled dynamics, (1) can be rewritten as

$$\begin{cases} \frac{di_d}{dt} = \frac{1}{L_{s0}}u_d - \frac{R_{s0}}{L_{s0}}i_d + \omega_e i_q + f_d + D_d \\ \frac{di_q}{dt} = \frac{1}{L_{s0}}u_q - \frac{R_{s0}}{L_{s0}}i_q - \omega_e i_d - \frac{1}{L_{s0}}\omega_e \psi_{f0} + f_q + D_q \end{cases} \tag{28}$$

where D_d and D_q denote the unknown interference items, including the inverter nonlinearity, unmodeled dynamics, etc. The disturbance f_d and f_q are expressed as

$$\begin{cases} f_d = \frac{1}{L_{s0}}(-\Delta R_s i_d - \Delta L_s \frac{di_d}{dt} + \omega_e \Delta L_s i_q) \\ f_q = \frac{1}{L_{s0}}(-\Delta R_s i_q - \Delta L_s \frac{di_q}{dt} - \omega_e \Delta L_s i_d - \omega_e \Delta\psi_f). \end{cases} \tag{29}$$

Furthermore, the ultralocal model of the current loop can be described as [9]

$$\begin{cases} \frac{di_d}{dt} = \alpha_s u_d + F_d \\ \frac{di_q}{dt} = \alpha_s u_q + F_q \end{cases} \tag{30}$$

where $\alpha_s = 1/L_s$, $\begin{cases} F_d = -\frac{R_{s0}}{L_{s0}}i_d + \omega_e i_q + f_d + D_d \\ F_q = -\frac{R_{s0}}{L_{s0}}i_q - \omega_e i_d + f_q + D_q. \end{cases}$

B. Design and Analysis of AESO

Taking q-axis as an example, by defining i_q and the total uncertainty F_q as the system states x_1 and x_2, respectively, the ultralocal model (30) can be rewritten as a typical nonlinear system as

$$\begin{cases} \dot{x}_1 = \alpha_s u_q + x_2 \\ \dot{x}_2 = M \end{cases} \tag{31}$$

where M represents the derivative of F_q. Then, the proposed AESO is given as

$$\begin{cases} e_1 = \hat{x}_1 - x_1 \\ \dot{\hat{x}}_1 = \alpha_s u_q + \hat{x}_2 - \beta_{01}(\omega_0)e_1 \\ \dot{\hat{x}}_2 = -\beta_{02}(\omega_0)e_1. \end{cases} \tag{32}$$

The adaptive bandwidth tuning scheme is designed as

$$\omega_0 = \omega_{0\min} + p(\omega_{0\max} - \omega_{0\min})\tanh\left(\varsigma|x_1 - \hat{x}_1|\right)^{\upsilon} \tag{33}$$

where p, ς, and υ are the variable gains, with tanh(*) the hyperbolic tangent function.

Assumption 1: Assume the system uncertainty F_q and its derivative $\dot{F}_q$ are both bounded.

Theorem 1: If Assumption 1 is satisfied, the estimation error of AESO (32) is also bounded.

Proof: For the convenience of parameter adjustment, define $\beta_{01}(\omega_0) = \beta_{01}\omega_0$, $\beta_{02}(\omega_0) = \beta_{02}\omega_0^2$, and extend the estimated error variable and consider $e_2 = \hat{x}_2 - x_2$, the error dynamics of the proposed AESO can be given as

$$\begin{bmatrix} \dot{e}_1 \\ \dot{e}_2 \end{bmatrix} = \begin{pmatrix} -\beta_{01}\omega_0 & 1 \\ -\beta_{02}\omega_0^2 & 0 \end{pmatrix} \begin{bmatrix} e_1 \\ e_2 \end{bmatrix} + \begin{bmatrix} 0 \\ 1 \end{bmatrix} M. \tag{34}$$

Let $\varepsilon_i = \frac{e_i}{\omega_0^{i-1}} \in \mathbb{R}^n$, $i = 1, 2$. Then, (34) can be written as

$$\dot{\boldsymbol{\varepsilon}} = \omega_0 \boldsymbol{A}\boldsymbol{\varepsilon} + \frac{\boldsymbol{B}}{\omega_0}M \tag{35}$$

where $\boldsymbol{\varepsilon} = [\varepsilon_1 \;\; \varepsilon_2]^T$, $\boldsymbol{A} = \begin{pmatrix} -\beta_{01} & 1 \\ -\beta_{02} & 0 \end{pmatrix}$, and $\boldsymbol{B} = [0 \;\; 1]^T$.

Solving (35), we can obtain

$$\varepsilon(t) = e^{\omega_0 At}\varepsilon(t_0) + \int_0^t e^{\omega_0 A(t-\tau)}\frac{BM}{\omega_0}d\tau. \tag{36}$$

Then, define

$$\begin{aligned} \varphi(t) &= \int_0^t e^{\omega_0 A(t-\tau)}\frac{BM}{\omega}d\tau \\ &= \frac{1}{\omega_0}\left(BF_q + \int_0^t BF_q\omega_0 Ae^{\omega_0 A(t-\tau)}d\tau\right) \end{aligned} \tag{37}$$

where $\varphi(t) = [\varphi_1 \;\; \varphi_2]^T \in \mathbb{R}^{2\times 1}$.

Moreover, according to Assumption 1, i.e., $|F_q| < R_F$, where R_F is a positive constant. Thus, we have

$$\begin{aligned} |\varphi_i(t)| &\leq \frac{1}{\omega_0}\left(R_F + \int_0^t BF_q\omega_0 Ae^{\omega_0 A(t-\tau)}d\tau\right) \\ &\leq \frac{R_F}{\omega_0}\sum_{j=1}^{2}|[e^{\omega_0 A(t)}]_{ij}| \end{aligned} \tag{38}$$

where $i = 1, 2$.

Since A can be Hurwitz when appropriate β_{01} and β_{02} are selected. Then, $\exists T_1 > 0$, when $t > T_1$ is satisfied, we have

$$|[e^{\omega_0 At}]_{ij}| \leq \frac{1}{\omega_0^k}(i, j = 1, 2) \tag{39}$$

where k is positive and $k > 2$.

Combining (38) and (39), we can obtain

$$|\varphi_i(t)| \leq \frac{2R_F}{\omega_0^{k+1}}. \tag{40}$$

According to (40), one can get

$$|[e^{\omega_0 At}\varepsilon(t_0)]_j| \leq \frac{1}{\omega_0^k}\sum_{j=1}^{2}|\varepsilon_j(0)|. \tag{41}$$

Then, according to (36), (40), and (41), we can obtain

$$|\varepsilon_j(t)| \leq \frac{2R_F}{\omega_0^{k+1}} + \frac{1}{\omega_0^k}\sum_{j=1}^{2}|\varepsilon_j(0)|. \tag{42}$$

Considering that $\varepsilon_i = \frac{e_i}{\omega_0^{i-1}} \in \mathbb{R}^n$, $i = 1, 2$, it yields

$$|e_i(t)| \leq f_i(i = 1, 2) \tag{43}$$

where $f_i = \begin{cases} \frac{2R_F}{\omega_0^{k+1}} + \frac{1}{\omega_0^k}\sum_{j=1}^{2}|\varepsilon_j(0)| & i = 1 \\ \frac{2R_F}{\omega_0^k} + \frac{1}{\omega_0^{k-1}}\sum_{j=1}^{2}|\varepsilon_j(0)| & i = 2. \end{cases}$

This completes the proof. In addition, for an electromechanical system, the total power is limited. Therefore, it is reasonable to assume the system uncertainty and its derivative are both bounded [33].

Then, based on (30) and (32), by using the forward Euler method, the proposed AESO for the current loop can be established as

$$\begin{cases} e_{d1}(k) = \hat{i}_d(k) - i_d(k) \\ \hat{i}_d(k+1) = \hat{i}_d(k) + T_s(\alpha_s u_d(k) + \hat{F}_d(k) \\ \qquad - \beta_{01}(\omega_0(k))e_{d1}(k)) \\ \hat{F}_d(k+1) = \hat{F}_d(k) - T_s\beta_{02}(\omega_0(k))e_{d1}(k) \end{cases} \tag{44}$$

$$\begin{cases} e_{q1}(k) = \hat{i}_q(k) - i_q(k) \\ \hat{i}_q(k+1) = \hat{i}_q(k) + T_s(\alpha_s u_q(k) + \hat{F}_q(k) \\ \qquad - \beta_{01}(\omega_0(k))e_{q1}(k)) \\ \hat{F}_q(k+1) = \hat{F}_q(k) - T_s\beta_{02}(\omega_0(k))e_{q1}(k) \end{cases} \tag{45}$$

where T_s is the sampling period of the current loop.

C. Voltage Calculation for AESO-MFPCC

By using the first-order Euler method, (30) can be discretized as

$$\begin{cases} u_d(k) = \frac{i_d(k+1) - i_d(k)}{\alpha_s T_s} - \frac{F_d(k)}{\alpha_s} \\ u_q(k) = \frac{i_q(k+1) - i_q(k)}{\alpha_s T_s} - \frac{F_q(k)}{\alpha_s}. \end{cases} \tag{46}$$

The one-step compensation is performed, and the reference voltage vector can be derived as

$$\begin{cases} u_d^{\text{ref}}(k+1) = \frac{i_d^{\text{ref}} - \hat{i}_d(k+1)}{\alpha_s T_s} - \frac{\hat{F}_d(k+1)}{\alpha_s} \\ u_q^{\text{ref}}(k+1) = \frac{i_q^{\text{ref}} - \hat{i}_q(k+1)}{\alpha_s T_s} - \frac{\hat{F}_q(k+1)}{\alpha_s} \end{cases} \tag{47}$$

where $\hat{i}_d(k+1)$, $\hat{i}_q(k+1)$, $\hat{F}_d(k+1)$, and $\hat{F}_q(k+1)$ can be obtained by (44) and (45). In addition, considering that the sampling period T_s is very short, it can be regarded that i_d^{ref}, i_q^{ref}, and ω_e^{ref} remain unchanged in two adjacent sampling periods, e.g., $i_d^{\text{ref}}(k+2) \approx i_d^{\text{ref}}(k)$, $i_q^{\text{ref}}(k+2) \approx i_q^{\text{ref}}(k)$, and $\omega_e^{\text{ref}}(k+2) \approx \omega_e^{\text{ref}}(k)$.

The diagram of the entire control scheme for SPMSM drives is shown in Fig. 4.

Remark 1: The highlight of the proposed AESO is that only the upper and lower limits of bandwidth need to be set; then, the observer gains can be adaptively adjusted according to the operating conditions to meet the different requirements of tracking accuracy and noise suppression under various operating conditions. In addition, numerical simulation and speed comparison experiments show that the NRL proposed in this article performs outstandingly in both convergence speed and chattering suppression. Thus, the NRL-based RSMSC can provide robust and remarkable speed control performance for MFPCC. More importantly, the control algorithms proposed in this article do not rely on motor parameters, making them suitable for more PMSM drive scenarios.

D. Control Parameters Selection

The discussion on the guidance to select the control parameters for the proposed algorithm is as follows: First, (23) indicates that the second term of NRL contains the switching function. Thus, the control gain k_2 must be greater than the upper boundary of the total disturbance to ensure stability [26]. However, an SMO is designed to observe the total disturbance of the speed loop. Hence, k_2 can be selected according to the upper bound of the observer error, effectively suppressing the chattering. Then, because θ and ρ are directly related to the chattering suppression performance, it is essential to coordinate the relationship between convergence velocity and chattering suppression. Besides, since Δ is the thickness of the boundary layer, the larger the thickness, the better the chattering suppression effect. However, the excessive value will deteriorate the dynamic response and robustness. In addition, larger values of k_1 and δ can also accelerate the convergence speed, while chattering will be increased. However, too small k_1 will lead to a deterioration in robustness. Furthermore, larger c and smaller ϕ can accelerate convergence speed and reduce tracking error. However, extreme values may lead to the saturation of the control input, which needs to be avoided. Finally, the parameters l and ν in SMO should be positive to ensure the convergence of the observation error. To sum up, based on the above analysis and experimental performance, the parameters of the comparative control methods can be demonstrated as

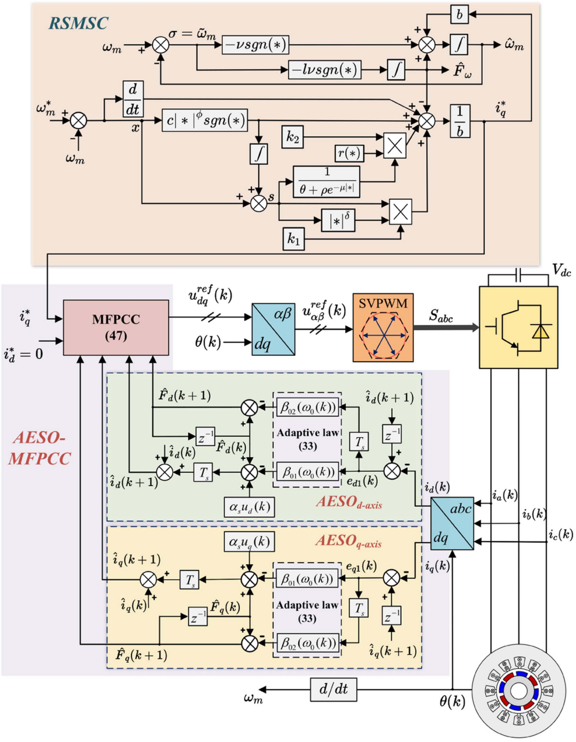

Fig. 4. Block diagram of the proposed control scheme.

The proposed NRL: $k_1 = 0.6$, $k_2 = 0.6$, $\theta = 0.1$, $\rho = 2$, $\mu = 1$, $\delta = 0.8$, $\Delta = 0.06$. TRL: $\eta_1 = 1$, $\eta_2 = 1.5$, $\lambda = 0.8$. EERL: $\eta_3 = 1.2$, $\eta_4 = 1.2$, $\alpha = 0.2$, $\beta = 5$, $\gamma = 0.7$. PI: $k_p = 0.0066$, $k_i = 0.0045$. Sliding surface: $c = 4$, $\phi = 0.6$. SMO: $l = -5$, $\nu = -50$. The proposed AESO: $\omega_{0\min} = 300$, $\omega_{0\max} = 1200$, $p = 0.8$, $\eta = 5$, $\upsilon = 0.6$.

V. EXPERIMENTAL VALIDATION

Fig. 5 shows the experimental platform of SPMSM, which consists of a test SPMSM, load motor, computer, and power

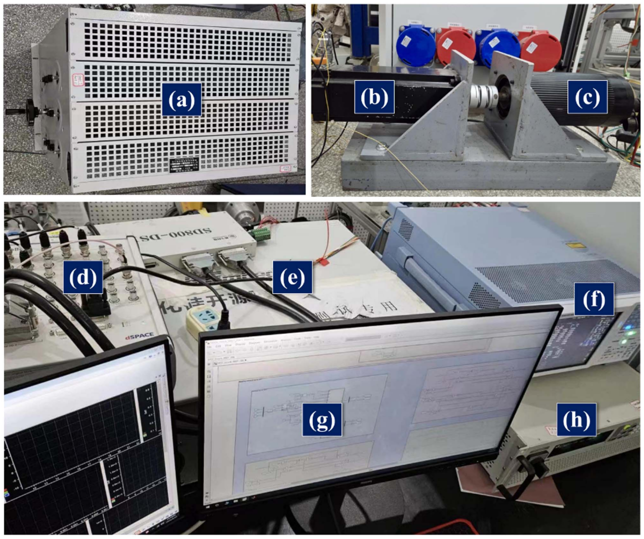

Fig. 5. Experimental platform. (a) Resistance box. (b) Load motor. (c) SPMSM. (d) dSPACE DS1202. (e) Power drive module. (f) Power analyzer. (g) Computer. (h) DC voltage source.

supply. The SVPWM with a 20 kHz switching frequency is utilized to generate the switching signals for the two-level VSI, composed of a SiC MOSFET module produced by Infineon (model FF11MR12W1M1). The dead time is set to 3.12 μs. The sampling frequencies of the speed and current loops are selected as 2 kHz and 20 kHz, respectively.

As for the speed loop, to verify the superiority of the proposed RSMSC, the traditional PI, TRL-based speed controller, and EERL-based speed controller are selected as the comparative speed control methods. Besides, all speed controllers adopt the proposed AESO-MFPCC strategy as the current control algorithm to ensure fairness. In addition, the designed SMO is utilized to compensate for the TRL-based speed controller and EERL-based speed controller. As for the current loop, all comparative current control methods adopt the proposed RSMSC as the speed control method to ensure fairness. The comparative current control methods are the conventional DPCC (denoted as Method 1), ESO-DPCC (proposed in [7], denoted as Method 2), ESO-MFPCC (proposed in [9], denoted as Method 3), and the proposed AESO-MFPCC (denoted as Method 4). In addition, all control methods are implemented in a dSPACE DS1202 real-time control system. The parameters of the test SPMSM are shown in Table I. The control parameter of α_s is selected as $\alpha_s = 667$.

TABLE I
PARAMETERS OF SPMSM

Descriptions	Parameters	Nominal Values
Rated Power	P_n [kW]	1.9
Rated Speed	n [r/min]	2200
DC Voltage	U_{dc} [V]	150
Number of Pole Pairs	n_p	2
Stator Resistance	R_s [Ω]	0.36
Inductance	$L_d = L_q$ [mH]	1.5
Flux linkage	ψ_f [Wb]	0.15
Rated Torque	T_L [$\mathrm{N \cdot m}$]	8

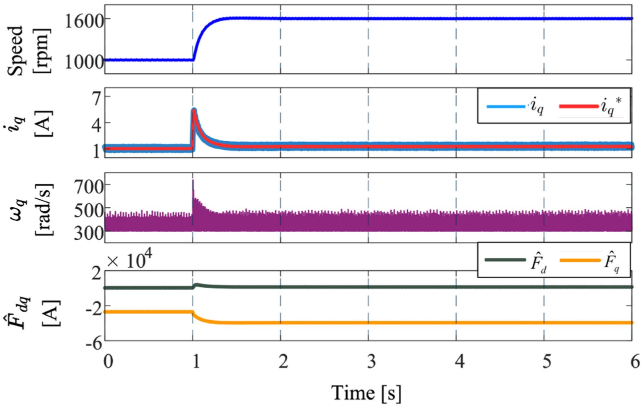

Fig. 6. Adaptive bandwidth and observed uncertainty of the proposed AESO-MFPCC under speed step response.

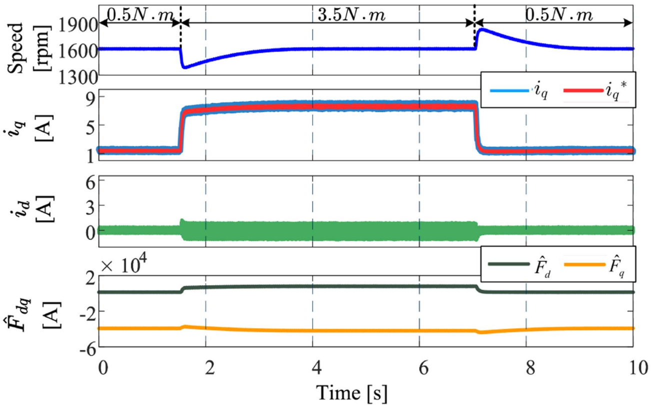

Fig. 7. Overall performance of the proposed control schemes under external load change.

A. Overall Performance of the Proposed Methods

As shown in Fig. 6, the adaptive gain of AESO increases when the reference speed suddenly changes, indicating that the proposed AESO can adjust the bandwidth according to the estimation error, significantly improving the current tracking performance. Moreover, when the system returns to the steady state, the bandwidth of AESO decreases so that a good noise suppression performance can be achieved. In addition, as can be seen from Fig. 7, F_q almost remains constant under different loads because it mainly depends on the PMSM speed, while the reference speed remains stable. Meanwhile, since F_d is affected by both speed and i_q, it will increase to a certain extent with the increase of q-axis current.

In addition, it is worth noting that when the dynamic process is over, i_q, i_d, F_d, F_q, and the actual speed return to steady states simultaneously, indicating the proposed methods exhibit excellent performance in both steady-state and dynamic response. In addition, to verify the superiority of AESO in balancing

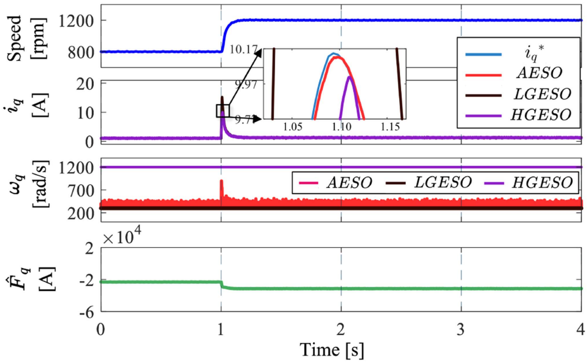

Fig. 8. Comparison of low-gain ESO, high-gain ESO, and AESO.

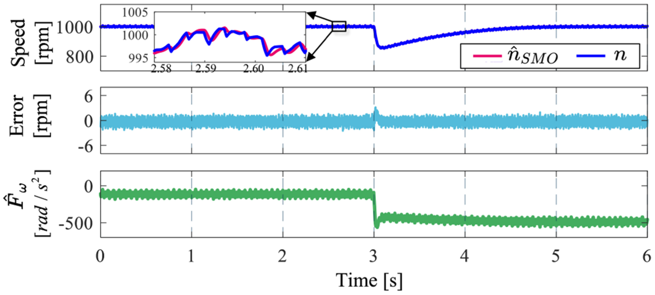

Fig. 9. SMO performance under load step response.

antidisturbance performance and noise suppression, the performance of high-gain ESO (HGESO), low-gain ESO (LGESO), and the proposed AESO is compared. The parameter settings for the three observers are as follows: HGESO bandwidth is 1200, LGESO bandwidth is 300, and the upper and lower limits of AESO bandwidth are 1200 and 300, respectively. The experimental results are shown in Fig. 8, in which the waveforms from top to bottom are the rotor speed, i_q^*, bandwidth, and F_q observation results. It can be seen that when the speed changes at $t = 1$ s, the reference current i_q^* also changes dramatically. The enlarged waveform diagram shows that in the dynamic situation, the observation error of LGESO is the largest, and AESO obtains the best observation performance. Moreover, the adaptive gain of AESO increases when the speed changes and decreases when the dynamic process ends. Accordingly, the bandwidth of the proposed AESO can be adjusted adaptively to coordinate the antidisturbance performance and noise suppression.

Moreover, the SMO performance is shown in Fig. 9, in which the waveforms from top to bottom are the rotor speed, speed observation error, and F_ω observation results. When the external load changes, the proposed RSMSC exhibits good robustness, and the proposed SMO performs well in the observation of speed and total disturbance. The oscillations in the observed total disturbance $\hat{F}_\omega$ converge to 0 in 0.05 s, and the steady-state observation error is within 0.6 rd/s.

B. Comparison of Speed Loop

The comparative experiment of the speed control methods consists of two tests. The first test is the speed command step response. In this test, the initial speed command is set to $n_{\text{ref}} = 1800$ r/min and suddenly changed to $n_{\text{ref}} = 2200$ r/min at $t = 2$ s. As shown in Fig. 10(d), the settling time of the proposed RSMSC is $t_s = 0.11$ s. As a comparison, the values of the comparative speed control methods are $t_s = 0.26$ s (PI), $t_s = 0.37$ s (TRL-based controller), and $t_s = 0.23$ s (EERL-based controller). Thus, it can be seen that the proposed RSMSC exhibits the best dynamic performance.

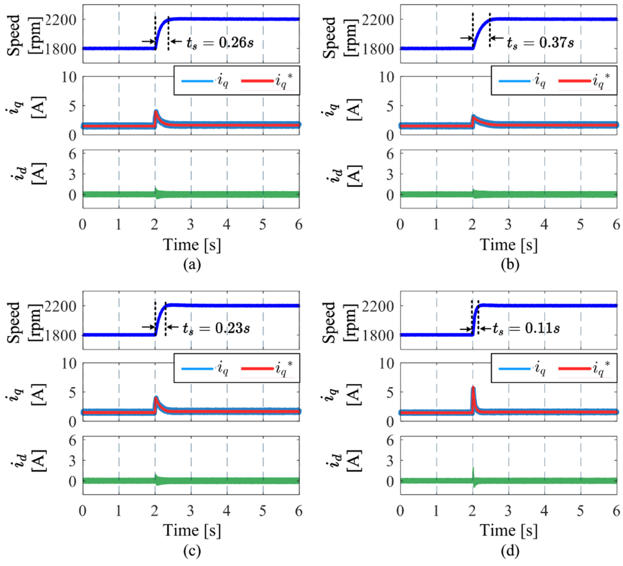

Fig. 10. Experimental results of four speed control methods with speed command step. (a) PI. (b) TRL-based controller. (c) EERL-based controller. (d) Proposed RSMSC.

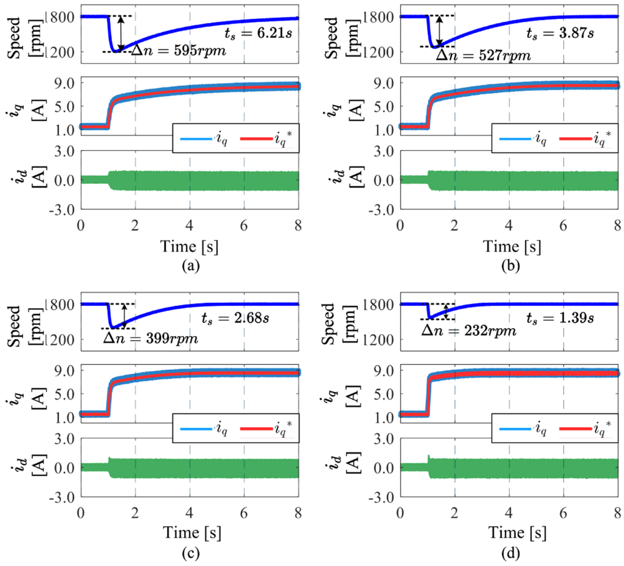

Fig. 11. Experimental results of four speed control methods with load step response. (a) PI. (b) TRL-based controller. (c) EERL-based controller. (d) Proposed RSMSC.

The second test is the load step response. In this test, the reference speed signal is set as $n_{\text{ref}} = 1800$ r/min, and the initial condition is set to $T_L = 0.5\ \text{N} \cdot \text{m}$ and suddenly changed to $T_L = 3.5\ \text{N} \cdot \text{m}$ at $t = 1$ s. As shown in Fig. 11(d), the speed drop and

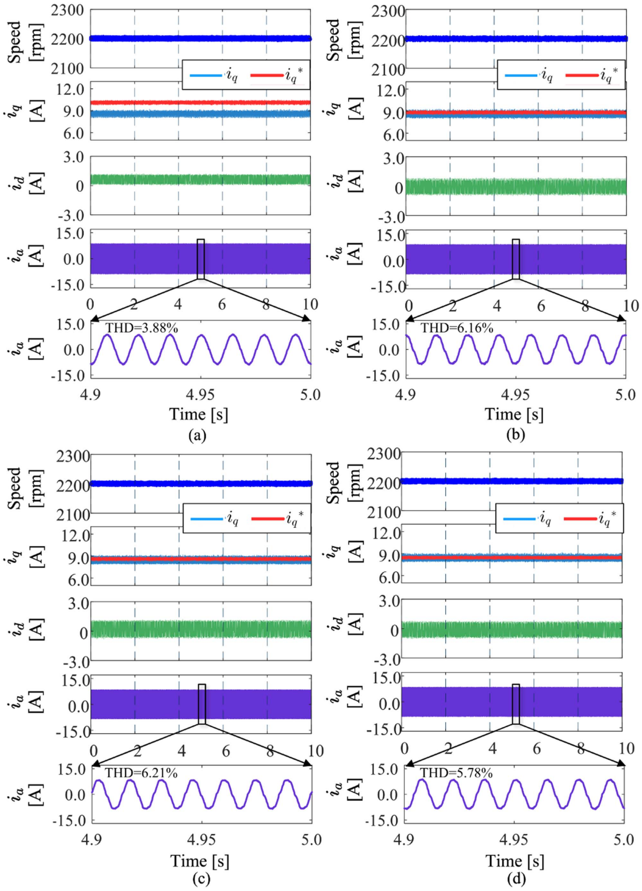

Fig. 12. Experimental results of four control methods at 2200 r/min under load with nominal motor parameter. (a) Method 1. (b) Method 2. (c) Method 3. (d) Method 4.

TABLE II
QUANTITATIVE RESULTS OF COMPARATIVE EXPERIMENT UNDER NOMINAL PARAMETER

Control Methods	Y_d(A)	Y_q(A)	$\bar{Y}$(A)	THD (%)
Method 1	1.08	1.58	1.33	3.88
Method 2	0.67	0.83	0.75	6.16
Method 3	0.68	0.86	0.82	6.21
Method 4	0.61	0.65	0.63	5.78

TABLE III
QUANTITATIVE RESULTS OF COMPARATIVE EXPERIMENT UNDER PARAMETER MISMATCH

Control methods	Parameter	Y_d(A)	Y_q(A)	$\bar{Y}$(A)	THD (%)
Method 1	$0.5L_s$	1.53	2.51	2.02	3.84
Method 2	$0.5L_s$	0.98	0.66	0.82	6.28
Method 3	$2\alpha_s$	0.92	0.53	0.73	6.32
Method 4	$2\alpha_s$	0.84	0.45	0.65	6.01

settling time of the proposed RSMSC are $\Delta n = 232$ r/min and $t_s = 1.39$ s, respectively. In contrast, the values of those of the comparative speed control methods are $\Delta n = 595$ r/min and $t_s = 6.21$ s (PI), $\Delta n = 527$ r/min and $t_s = 3.87$ s (TRL-based controller), and $\Delta n = 399$ r/min and $t_s = 2.68$ s (EERL-based controller). Accordingly, the proposed RSMSC achieves the best dynamic performance and robustness.

C. Comparison of Current Loop

1) Steady-state performance: Fig. 12 shows the steady-state results of the four methods under nominal motor parameters. The speed command is $n_{\text{ref}} = 2200$ r/min. As shown in Fig. 12(a), to the conventional DPCC, an obvious current tracking error exists in q-axis current because of the disturbances such as inverter nonlinearity, dead time, and unmodeled dynamics, etc., which is consistent with the analysis in [30]. Besides, the static error also exists in the d-axis current. Due to the ESO compensation in Method 2, i_q can keep up with the reference signal i_q^*, as shown in Fig. 12(b). Meanwhile, Fig. 12(c) shows the experimental results of Method 3. It can be seen that the tracking performance of the q-axis current is generally good, but there is a slight error between i_q^* and i_q. Then, the waveforms of Method 4 are shown in Fig. 12(d), which exhibits the best tracking performance. In addition, to demonstrate the steady-state performance more intuitively, two indices reflecting the current ripple are introduced as follows [34]:

$$Y_m = \sqrt{\frac{1}{n}\sum_{j=1}^{m}\left(i_m^* - i_m\right)^2}, \quad m = d, q. \tag{48}$$

$$\bar{Y} = (Y_d + Y_q)/2 \tag{49}$$

where n denotes the number of sampling points.

The quantitative experimental data indexes corresponding to Fig. 12 are shown in Table II.

Thus, it can be concluded from Fig. 12 and Table II that the average current ripple index of the dq-axis and the THD of stator current i_a of Method 4 are 0.63 and 5.78%, respectively, which are smaller than those of Method 2 (0.75 and 6.16%) and Method 3 (0.82 and 6.21%). Although the THD index of Method 1 is 3.88%, the average current ripple index reaches 1.33, 2.06 times that of Method 4. Thus, the proposed method performs best in current tracking and steady-state conditions. Specifically, compared with Method 3, because the proposed AESO can dynamically adjust the bandwidth, and the observation uncertainty and current are more accurate, Method 4 obtains a better performance.

In addition, it is difficult to change the value of the inductance parameter online in real SPMSM applications, the parameter variation test is carried out by changing its value in the control methods. Note that Methods 3 and 4 are model-free algorithms, so theoretically, they do not include motor parameters. However, the value of α_s is related to inductance L_s to a certain extent, so the inductance variation is simulated by changing the value of α_s [34]. For example, the nominal value of the inductance of the test SPMSM in this article is 1.5 mH, so the value adopted in the controller is $L_s = 0.75$ mH to denote that inductance is 50% variation ($\alpha_s = 1333$ is set in Method 3 and Method 4).

The experiment waveforms and quantitative results are shown in Fig. 13 and Table III, respectively. It can be seen that when the control parameters become twice the original, the performance of the proposed control algorithm remains almost unchanged.

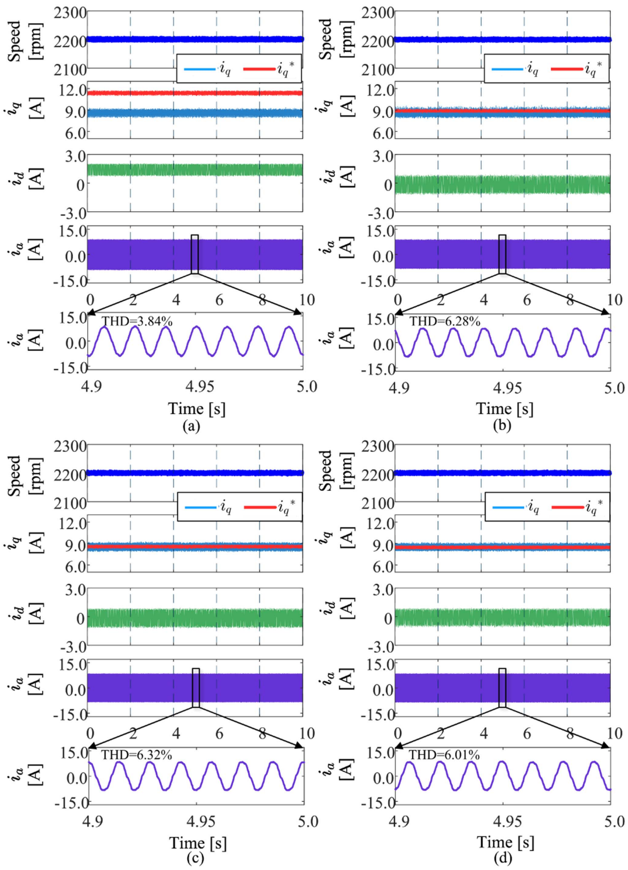

Fig. 13. Experimental results of four control methods at 2200 r/min under load with mismatched parameter $50\% L_s$ ($2\alpha_s$ for Method 3 and Method 4). (a) Method 1. (b) Method 2. (c) Method 3. (d) Method 4.

This is because the designed AESO accurately estimates all system uncertainties (including perturbations caused by parameter changes) in each sampling period and feeds back online to the controller, fundamentally eliminating the influence of parameter perturbations on control performance. The experimental results are consistent with the above theoretical analysis. The current ripple and THD values of the other three methods are larger than those of the proposed algorithm, which shows that the proposed algorithm still exhibits the best steady-state performance and the strongest robustness under the working condition of the parameter variation.

Remark 2: Note that for Method 4, the average current ripple index of the dq-axis with nominal and mismatched parameters is 0.63 A and 0.65 A, respectively, which are very close, indicating that the proposed control scheme exhibits strong robustness against parameter mismatch.

2) Dynamic performance: The first dynamic test is the i_q^* jump response. In this test, the speed outer loop is discarded, and the initial condition of the reference current signal is set to $i_q^* = 2$ A and suddenly changed to $i_q^* = 6$ A. To better illustrate the impact of the designed AESO on control performance, experiments of Method 3 are conducted under two different bandwidths of $\omega_0 = 300$ and $\omega_0 = 1200$, respectively. As shown in Fig. 14(d), when $\omega_0 = 1200$ is adopted, the current tracking is achieved after 1 ms, which is greatly accelerated. However, an obvious overshoot occurs, with the value larger than 4.8 A. In addition, when $\omega_0 = 300$ is adopted, the current tracking is achieved after 11 ms, which is relatively long, as shown in Fig. 14(e). Therefore, the experiment results indicate that Method 3 needs to choose an appropriate bandwidth to balance the performance of response time and overshoot. In contrast, for Method 4, the current tracking is achieved after 5 ms, and the overshoot value is 0.388 A, with a good current ripple performance, as shown in Fig. 14(f).

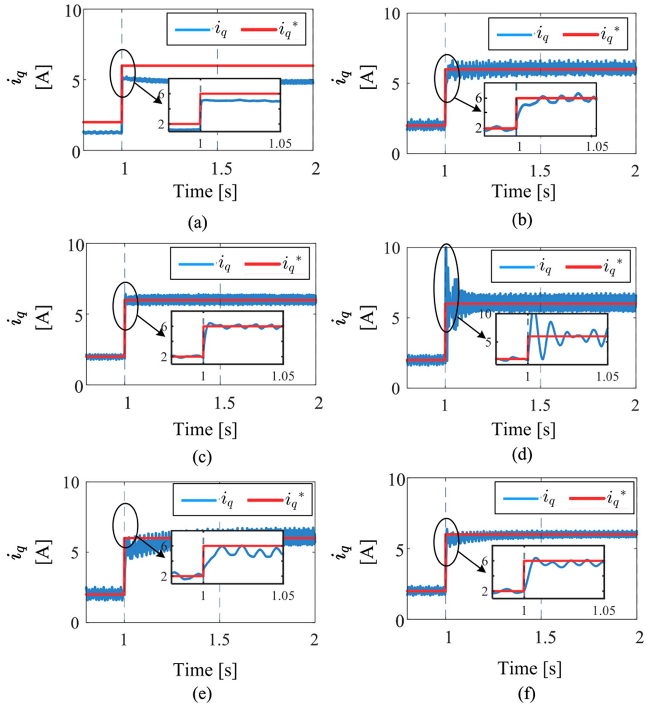

Fig. 14. Experimental results of i_q^* step response. (a) Method 1. (b) Method 2 with high gain ESO. (c) Method 2 with low gain ESO. (d) Method 3 with high gain ESO. (e) Method 3 with low gain ESO. (f) Method 4.

In addition, for Method 2, because it also adopts the traditional ESO, experiments are conducted under two different bandwidths of $\omega_{0\min} = 300$ and $\omega_{0\max} = 1200$, respectively. It can be seen from Fig. 14(b) that when the bandwidth of ESO is set to 300, the response time is 15 ms. Meanwhile, when the bandwidth is set to 1200, overshoot also occurs, and the value is 0.48 A, which is less than Method 3. This is because Method 3, as a model-free control algorithm, relies more on the observation results of the observer.

The second dynamic test is the load step response for Method 3 and Method 4. Firstly, the initial condition is set to $T_L = 0.5\ \text{N} \cdot \text{m}$ and suddenly changed to $T_L = 1.8\ \text{N} \cdot \text{m}$. The reference speed is $n_{\text{ref}} = 1000$ r/min. It can be seen in Fig. 15 that both Method 3 and Method 4 obtain satisfactory performance of dynamic current tracking when there is a sudden change in load torque. Then, the initial condition is set to $T_L = 0.5\ \text{N} \cdot \text{m}$ and suddenly changed to $T_L = 3.5\ \text{N} \cdot \text{m}$. The reference speed is $n_{\text{ref}} = 2200$ r/min. Similarly, the current tracking performance of both methods is good. The difference is that the maximum i_d of Method 3 reaches 2.27 A, while that of Method 4 is 1.18 A, which is nearly half of Method 3, as shown in Fig. 15(c) and (d).

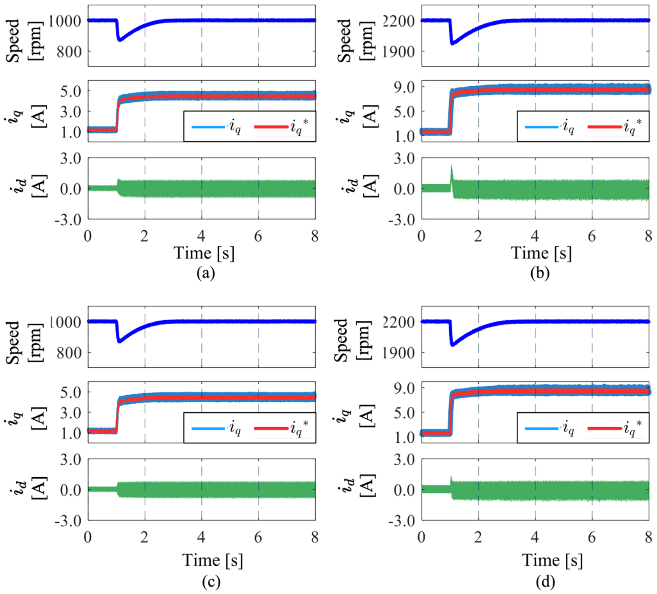

Fig. 15. The results of load step with nominal parameter. (a) Method 3 under $n_{\mathrm{ref}} = 1000$ r/min. (b) Method 3 under $n_{\mathrm{ref}} = 2200$ r/min. (c) Method 4 under $n_{\mathrm{ref}} = 1000$ r/min. (d) Method 4 under $n_{\mathrm{ref}} = 2200$ r/min.

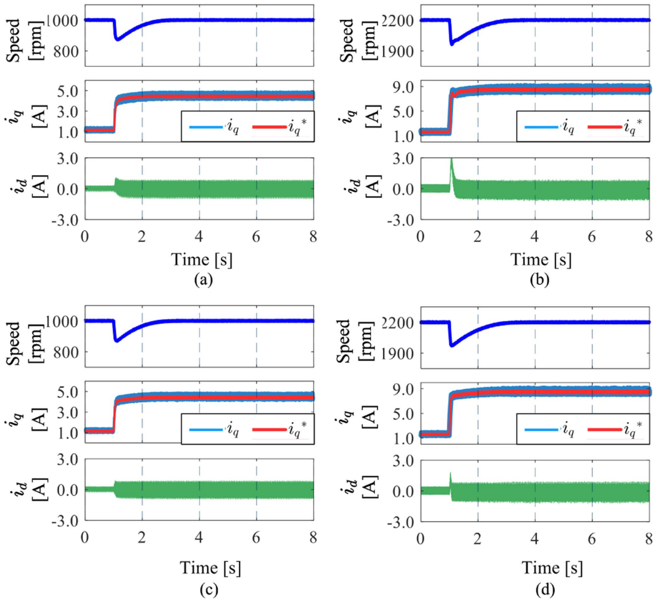

Fig. 16. Results of load step with mismatched parameter $2\alpha_s$ for Method 3 and Method 4. (a) Method 3 under $n_{\mathrm{ref}} = 1000$ r/min. (b) Method 3 under $n_{\mathrm{ref}} =$ 2200 r/min. (c) Method 4 under $n_{\mathrm{ref}} = 1000$ r/min. (d) Method 4 under $n_{\mathrm{ref}} =$ 2200 r/min.

In addition, Fig. 16 shows the performance of the load torque response of Method 3 and Method 4 with the parameter mismatch of $2\alpha_s$. Then, the waveforms of the q-axis current tracking error with nominal and mismatched parameters are shown in Figs. 17 and 18, respectively. It can be noted that an obvious tracking error in the dynamic process exists in Method 3 with the nominal parameter, and the value exceeds 0.85 A, as shown in Fig. 17(b). Moreover, in Fig. 18(b), the error increases to 1.02 A when the parameter mismatch occurs. In contrast, the tracking error of Method 4 remains stable under four operating conditions. As shown in Fig. 18(d), the maximum tracking error is 0.72 A when the parameter mismatch occurs. Thus, it is proved that the proposed method shows remarkable robustness against parameter perturbation.

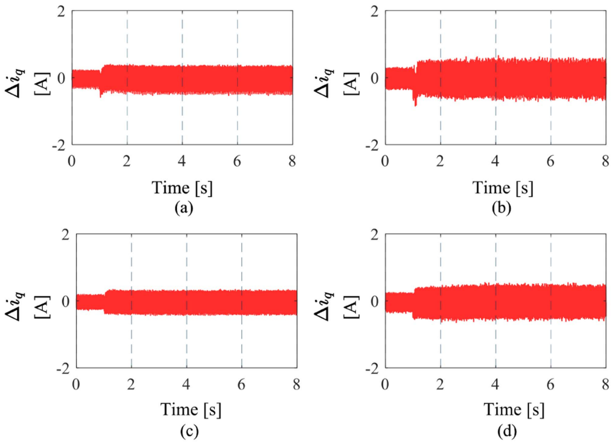

Fig. 17. Current tracking error with nominal parameter. (a) Method 3 under $n_{\mathrm{ref}} = 1000$ r/min. (b) Method 3 under $n_{\mathrm{ref}} = 2200$ r/min. (c) Method 4 under $n_{\mathrm{ref}} = 1000$ r/min. (d) Method 4 under $n_{\mathrm{ref}} = 2200$ r/min.

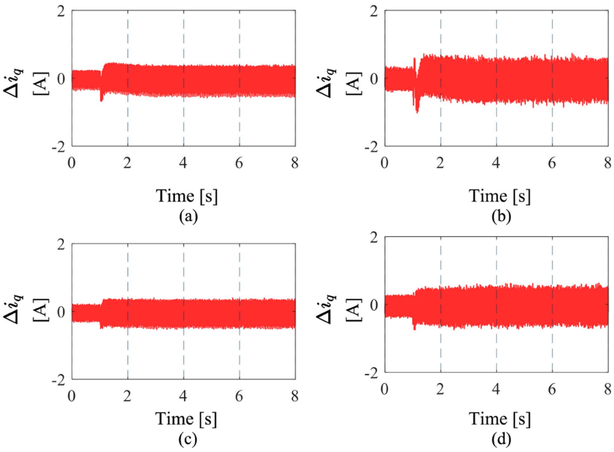

Fig. 18. Current tracking error with mismatched parameter $2\alpha_s$ for Method 3 and Method 4. (a) Method 3 under $n_{\mathrm{ref}} = 1000$ r/min. (b) Method 3 under $n_{\mathrm{ref}} = 2200$ r/min. (c) Method 4 under $n_{\mathrm{ref}} = 1000$ r/min. (d) Method 4 under $n_{\mathrm{ref}} = 2200$ r/min.

Remark 3: According to the experimental results, the proposed AESO significantly coordinates the dynamic response and the overshoot performance. In the load torque response test under parameter mismatch, the maximum tracking error of the proposed AESO-MFPCC is 70.5% of that of the ESO-MFPCC. In addition, the proposed SMO accurately estimates the lumped disturbance and compensates for the speed controller, effectively promoting dynamic performance and robustness.

D. Comparison With Existing AESOs

To demonstrate the superiority of the proposed AESO, comparative experiments are conducted with the AESO proposed in [13] and [16]. In this test, the speed outer loop is discarded

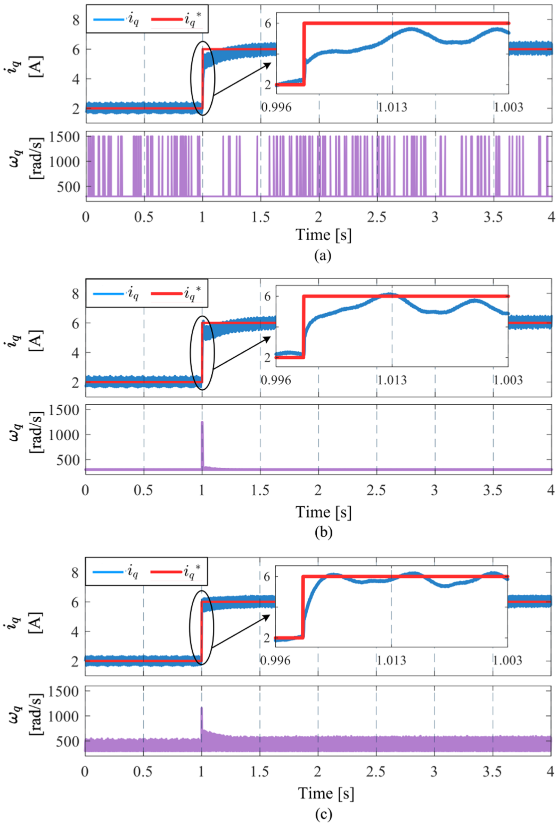

Fig. 19. Experimental results of i_q^* step response with nominal motor parameter. (a) AESO in [13]. (b) AESO in [16]. (c) Proposed AESO.

TABLE IV
COMPARISON OF THE PROPOSED METHOD WITH OTHER METHODS

Descriptions	TRL in [28]	TRL in [29]	NRL
Execution Time	1.07 μs	1.30 μs	1.36 μs

and the MFPCC is compensated by the AESO in [13], in [16], and in this article, respectively. The initial condition is set to $i_q^* = 2$ A and suddenly changed to $i_q^* = 6$ A at $t = 1$ s. To ensure fairness, the three AESOs are developed with the same bandwidth limits, e.g., $\omega_{0\min} = 300$ and $\omega_{0\max} = 1500$. The results under the nominal parameter are shown in Fig. 19. It can be seen in Fig. 19(c) that due to the compensation of the AESO proposed in this article, the tracking was achieved after 0.004 s, which is faster than the other methods (0.015 s and 0.011 s, respectively). Furthermore, the results under parameter mismatch are shown in Fig. 20. As seen in Fig. 20(a), an obvious tracking error exists at the beginning of the transient state, and the tracking was achieved after 0.32 s. As seen in Fig. 20(b), the tracking is achieved after 0.29 s. In contrast, the proposed method exhibits a remarkably excellent dynamic performance, which only takes 0.006 s to realize the current tracking, as shown in Fig. 20(c).

E. Computational Burden Comparison

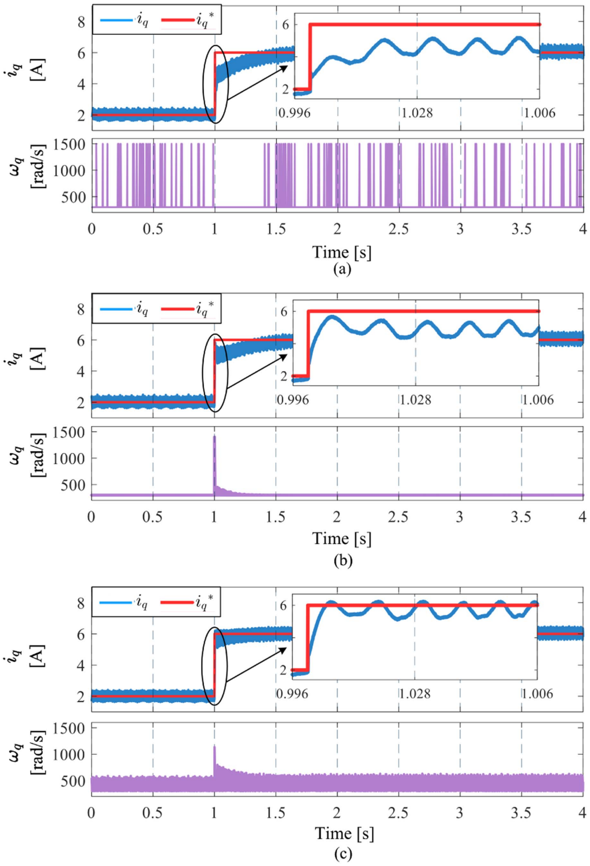

Fig. 20. Experimental results of i_q^* step response with mismatched parameter $2\alpha_s$. (a) AESO in [13]. (b) AESO in [16]. (c) Proposed AESO.

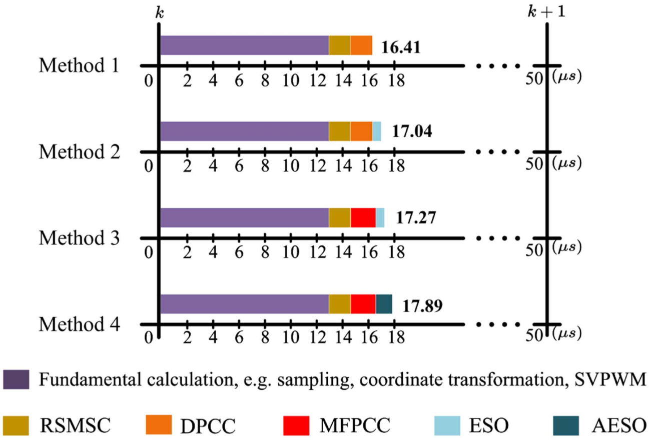

Fig. 21. Execution time of each part code of the 4 predictive current control methods.

The execution time on the digital controller of each method is compared and analyzed. As shown in Table IV, because more control parameters are contained and a boundary layer is added, the execution time of the proposed NRL is 1.36 μs, which is a little more than TRL in [28] and EERL in [29]. Besides, the execution time of PI is 0.69 μs.

In addition, the execution time of comparative predictive current methods is shown in Fig. 21. The sampling period of the current loop in this article is 50 μs. Note that all comparative methods can be accomplished in one sampling period. Due to the same speed controller being adopted, the difference in execution time mainly lies in the current control methods. The execution time for DPCC and MFPCC is 1.68 μs and 1.91 μs, respectively. MFPCC is essentially an optimized deadbeat control strategy, and it utilizes an ultralocal model instead of the physical model to generate the command voltage vector. Moreover, the execution time of the ESO is 0.63 μs. As a comparison, due to the addition of the adaptive bandwidth tuning algorithm, the execution time of AESO is 1.25 μs.

Accordingly, the proposed speed and predictive current control strategies have longer execution times than their respective comparative methods. When adopting the proposed speed and current control methods simultaneously, the execution time is 17.89 μs, less than half of the sampling period, and it does not add too much computation to the digital implementation.

VI. CONCLUSION

This article proposes novel AESO-MFPCC and RSMSC control methods to improve the steady-state, dynamic performance, and robustness of conventional ESO-based MFPCC. Due to the adaptive bandwidth tuning scheme based on the estimated error, the antidisturbance capability and noise suppression performance are balanced. Accordingly, the steady-state tracking accuracy, dynamic performance, and robustness to parameter perturbation of the proposed AESO-MFPCC are significantly improved. Moreover, the NRL-based RSMSC is developed to replace traditional PI as the speed controller for AESO-MFPCC. The comprehensive experimental results demonstrate the superiority of the proposed control methods. For future work, the noise suppression issue will be taken into account. In addition, a thorough analysis of the current loop disturbances caused by magnetic saturation and the dead time will be conducted, and an enhanced ESO is considered to be developed to attenuate the periodic disturbances.

REFERENCES

[1] X. Liu, H. Chen, J. Zhao, and A. Belahcen, "Research on the performances and parameters of interior PMSM used for electric vehicles," *IEEE Trans. Ind. Electron.*, vol. 63, no. 6, pp. 3533–3545, Jun. 2016.

[2] T. Zhao, S. Wu, and S. Cui, "Multiphase PMSM with asymmetric windings for more electric aircraft," *IEEE Trans. Transp. Electrific.*, vol. 6, no. 4, pp. 1592–1602, Dec. 2020.

[3] M. Tian, B. Wang, Y. Yu, Q. Dong, and D. Xu, "Adaptive active disturbance rejection control for uncertain current ripples suppression of PMSM drives," *IEEE Trans. Ind. Electron.*, vol. 71, no. 3, pp. 2320–2331, Mar. 2024.

[4] X. Sun, J. Cao, G. Lei, Y. Guo, and J. Zhu, "A composite sliding mode control for SPMSM drives based on a new hybrid reaching law with disturbance compensation," *IEEE Trans. Transp. Electrific.*, vol. 7, no. 3, pp. 1427–1436, Sep. 2021.

[5] Y. Wang, X. Wu, C. Dang, and W. Xie, "A desired voltage vector based MPTC strategy for PMSM with optimized switching pattern," *IEEE Trans. Energy Convers.*, vol. 37, no. 2, pp. 970–977, Jun. 2022.

[6] F. Wang, L. He, and J. Rodríguez, "A robust predictive speed control for SPMSM systems using a sliding mode gradient descent disturbance observer," *IEEE Trans. Energy Convers.*, vol. 38, no. 1, pp. 540–549, Mar. 2023.

[7] X. Li, S. Zhang, C. Zhang, Y. Zhou, and C. Zhang, "An improved deadbeat predictive current control scheme for open-winding permanent magnet synchronous motors drives with disturbance observer," *IEEE Trans. Power Electron.*, vol. 36, no. 4, pp. 4622–4632, Apr. 2021.

[8] L. Yan and F. Wang, "Observer-predictor-based predictive torque control of induction machine for robustness improvement," *IEEE Trans. Power Electron.*, vol. 36, no. 8, pp. 9477–9486, Aug. 2021.

[9] Y. Zhang, J. Jin, and L. Huang, "Model-free predictive current control of PMSM drives based on extended state observer using ultralocal model," *IEEE Trans. Ind. Electron.*, vol. 68, no. 2, pp. 993–1003, Feb. 2021.

[10] X. Yuan, Y. Zuo, Y. Fan, and C. H. T. Lee, "Model-free predictive current control of SPMSM drives using extended state observer," *IEEE Trans. Ind. Electron.*, vol. 69, no. 7, pp. 6540–6550, Jul. 2022.

[11] W. Wei et al., "A scalable-bandwidth extended state observer-based adaptive sliding-mode control for the dissolved oxygen in a wastewater treatment process," *IEEE Trans. Cybern.*, vol. 52, no. 12, pp. 13448–13457, Dec. 2022.

[12] K. Rsetam, M. Al-Rawi, and Z. Cao, "Robust adaptive active disturbance rejection control of an electric furnace using additional continuous sliding mode component," *ISA Trans.*, vol. 130, pp. 152–162, 2022.

[13] Q. Qin, G. Gao, and J. Zhong, "Finite-time adaptive extended state observer-based dynamic sliding mode control for hybrid robots," *IEEE Trans. Circuits Syst. II, Exp. Briefs*, vol. 69, no. 9, pp. 3784–3788, Sep. 2022.

[14] K. Rsetam, Y. Zheng, Z. Cao, and Z. Man, "Adaptive active disturbance rejection control for vehicle steer-by-wire under communication time delays," *Appl. Syst. Innov.*, vol. 7, no. 2, pp. 2524–2539, 2024.

[15] Y. Zhong, H. Lin, J. Wang, and H. Yang, "Sensorless control of variable flux memory machines based on improved extended EMF model and adaptive extended state observer," *IEEE Trans. Transport. Electrific.*, vol. 10, no. 3, pp. 5624–5635, Sep. 2024.

[16] X. Sun, Z. Su, G. Lei, Y. Cai, and M. Yao, "Adaptive model-free predictive current control for SPMSM drives with optimal virtual vector modulation," *IEEE/ASME Trans. Mechatron.*, vol. 29, no. 4, pp. 2569–2578, Aug. 2024.

[17] Y. Lu, W. Xiao, and D. D.-C. Lu, "Optimal dynamic and steady-state performance of PV-interfaced converters using adaptive observers," *IEEE Trans. Circuits Syst. II, Exp. Briefs*, vol. 69, no. 12, pp. 4909–4913, Dec. 2022.

[18] J. Wang, Y. Liu, J. Yang, F. Wang, and J. Rodríguez, "Adaptive integral extended state observer-based improved multistep FCS-MPCC for PMSM," *IEEE Trans. Power Electron.*, vol. 38, no. 9, pp. 11260–11276, Sep. 2023.

[19] Z. Liu, X. Huang, Q. Hu, G. Yang, Y. Wang, and J. Shen, "Model-free predictive current control of PMSM using modified extended state observer," *IEEE Trans. Power Electron.*, vol. 40, no. 1, pp. 679–690, Jan. 2025.

[20] S. Zhu et al., "Robust speed control of electrical drives with reduced ripple using adaptive switching high-order extended state observer," *IEEE Trans. Power Electron.*, vol. 37, no. 2, pp. 2009–2020, Feb. 2022.

[21] L. Yang, H. Li, J. Huang, Z. Zheng, and H. Zhao, "Model predictive direct speed control with novel cost function for SMPMSM drives," *IEEE Trans. Power Electron.*, vol. 37, no. 8, pp. 9586–9595, Aug. 2022.

[22] S.-K. Kim, K.-G. Lee, and K.-B. Lee, "Singularity-free adaptive speed tracking control for uncertain permanent magnet synchronous motor," *IEEE Trans. Power Electron.*, vol. 31, no. 2, pp. 1692–1701, Feb. 2016.

[23] Y. Zuo, X. Zhu, L. Quan, C. Zhang, Y. Du, and Z. Xiang, "Active disturbance rejection controller for speed control of electrical drives using phase-locking loop observer," *IEEE Trans. Ind. Electron.*, vol. 66, no. 3, pp. 1748–1759, Mar. 2019.

[24] C. Dang et al., "An improved adaptive sliding mode speed control of PMSM drives with an extended state observeran improved adaptive sliding mode speed control of PMSM drives with an extended state observer," *IEEE Trans. Energy Convers.*, vol. 39, no. 4, pp. 2349–2361, Dec. 2024.

[25] Y. Zheng, Z. Cao, K. Rsetam, Z. Man, and S. Wang, "Extreme learning machine-based super-twisting integral terminal sliding mode speed control of permanent magnet synchronous motors," *IET Control Theory Appl.*, vol. 18, no. 18, pp. 2524–2539, 2024.

[26] T. H. Nguyen, T. T. Nguyen, V. Q. Nguyen, K. M. Le, H. N. Tran, and J. W. Jeon, "An adaptive sliding-mode controller with a modified reduced-order proportional integral observer for speed regulation of a permanent magnet synchronous motor," *IEEE Trans. Ind. Electron.*, vol. 69, no. 7, pp. 7181–7191, Jul. 2022.

[27] B. Xu, L. Zhang, and W. Ji, "Improved non-singular fast terminal sliding mode control with disturbance observer for PMSM drives," *IEEE Trans. Transp. Electrific.*, vol. 7, no. 4, pp. 2753–2762, Dec. 2021.

[28] H. Wang et al., "Continuous fast nonsingular terminal sliding mode control of automotive electronic throttle systems using finite-time exact observer," *IEEE Trans. Ind. Electron.*, vol. 65, no. 9, pp. 7160–7172, Sep. 2018.

[29] S. M. Mozayan, M. Saad, H. Vahedi, H. Fortin-Blanchette, and M. Soltani, "Sliding mode control of PMSG wind turbine based on enhanced exponential reaching law," *IEEE Trans. Ind. Electron.*, vol. 63, no. 10, pp. 6148–6159, Oct. 2016.

[30] B. Wang, C. Luo, Y. Yu, G. Wang, and D. Xu, "Antidisturbance speed control for induction machine drives using high-order fast terminal sliding-mode load torque observer," *IEEE Trans. Power Electron.*, vol. 33, no. 9, pp. 7927–7937, Sep. 2018.

[31] C. Lian, F. Xiao, S. Gao, and J. Liu, "Load torque and moment of inertia identification for permanent magnet synchronous motor drives based on sliding mode observer," *IEEE Trans. Power Electron.*, vol. 34, no. 6, pp. 5675–5683, Jun. 2019.

[32] V. Utkin, "Variable structure systems with sliding modes," *IEEE Trans. Autom. Control*, vol. 22, no. 2, pp. 212–222, Apr. 1977.

[33] L. Zhao, S. Gu, J. Zhang, and S. Li, "Finite-time trajectory tracking control for rodless pneumatic cylinder systems with disturbances," *IEEE Trans. Ind. Electron.*, vol. 69, no. 4, pp. 4137–4147, Apr. 2022.

[34] B. Luo, X. Yang, and Y. Zhou, "Model-free predictive current control of permanent magnet synchronous motor based on estimation of current variations," *IEEE Trans. Ind. Electron.*, vol. 71, no. 8, pp. 8395–8405, Aug. 2024.

Changliang Dang was born in Shaanxi, China. He received the B.S. degree in electrical engineering from Southeast University, Nanjing, China, in 2006. He is currently working toward the Ph.D. degree in electrical engineering with Northwestern Polytechnical University, Xi'an, China.

From 2006 to 2008, he worked with Toshiba Transformer Company Ltd. in Changzhou, China. From 2011 to 2018, he worked with the Baoji University of Arts and Sciences, Baoji, China. His research interests include advanced control of power electronics and drives.

Manfeng Dou (Member, IEEE) received the M.S. and Ph.D. degrees in electrical engineering from Northwestern Polytechnical University (NPU), Xi'an, China, in 1991 and 1998, respectively.

From 1998 to 2005, he was an Associate Professor with NPU. In 2005, he became a Full Professor with NPU. He is the Vice Director of the Institute of Rare Earth Permanent Magnet (REPM) Electric Machine and Control Technology, NPU. His research interests include electrical machine design, analysis of electromagnetic fields, motion control technology, and intelligent control.

Dr. Dou was the recipient of the second prize of the China National Invention Award in 1993, the second prize of the China National Defense Science and Technology Progress Award in 2018, and the Youth Science Award of Shaanxi Province, China, in 2004.

Shuhao Yan was born in Henan, China, in 1994. He received the M.S. degree in electrical engineering from Henan Polytechnic University, Henan, in 2020. He is currently working toward the Ph.D. degree in control science and engineering with Northwestern Polytechnical University, Xi'an, China.

His research interests include robust control technology for permanent magnet synchronous motors.

Mengxi Dang was born in Shaanxi, China, in 1996. She received B.S. degree in electrical engineering from Xi'an University of Architecture and Technology, China, in 2018, and the master's degree in electrical engineering, in 2021, from Northwestern Polytechnical University (NPU), Xi'an, China, where she is currently working toward the Ph.D. degree in electrical engineering.

Her main research interests include optimization of high-performance PMSM and advanced control of PMSM drive systems.

Dongdong Zhao (Member, IEEE) received the B.Eng. degree in information antagonizing technology from Northwestern Polytechnical University (NPU), Xi'an, China, in 2008, and the doctorate degree in electrical engineering from the University of Technology of Belfort-Montbéliard (UTBM), Belfort, France, in 2014.

Since 2014, he has been an Associate Professor with NPU. He is currently a Professor with NPU. His research interests include fuel cell system modeling and control, power electronics, and motor drives.

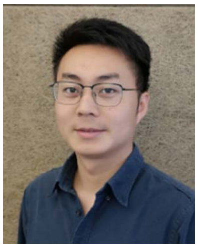

Zhiguang Hua (Member, IEEE) received the B.S. degree in electrical engineering and automation from Xi'an University of Technology (XAUT), Xi'an, China, in 2015, the M.S. degree in electrical engineering from Northwestern Polytechnical University (NPU), Xi'an, in 2018, and the Ph.D. degree in electrical engineering from the University of Technology of Belfort-Montbéliard (UTBM), Belfort, France, in 2021.

He separately finished his dual Postdoctoral Research with UTBM and NPU in 2022 and 2024, respectively. He was supported by the National Natural Science Foundation of China (NSFC) in 2023. Since 2024, he is a Full Professor with NPU. His main research interests include prognostic and health management of fuel cells, and permanent magnet synchronous motor control.